

Article

Development of a Bidirectional DC–DC Converter with Rapid Energy Bidirectional Transition Technology

Hsuan Liao ^{1,*}, Yi-Tsung Chen ¹, Linda Chen ² and Jiann-Fuh Chen ¹

¹ Department of Electrical and Electronics Engineering, National Cheng Kung University, Tainan City 701, Taiwan; cow965511@gmail.com (Y.-T.C.); chenjf@mail.ncku.edu.tw (J.-F.C.)

² Department of Electrical and Computer Engineering, University of Canterbury, Christchurch 8041, New Zealand; lindsay.chen@canterbury.ac.nz

* Correspondence: n28064046@gs.ncku.edu.tw

Abstract: Bidirectional DC–DC converters are key devices in the DC distribution system and the energy storage system (ESS). It is important to consider the safety of the elements in the converter for rapid conversion of the power direction. Damages may occur to the power-related components in the circuit if the direction of the inductor current or the capacitor voltage changes instantaneously. To make the power flow change smoothly and quickly, this research proposed a bidirectional DC–DC converter with rapid energy transition technology implemented in the circuit architecture. The rapid energy bidirectional transition technology added a resonance path based on the LC resonant circuit, allowing rapid energy conversion through the resonance path. Therefore, the energy in the energy storage element could be quickly converted without causing circuit surges. Analyses of the converter operating in the step-up mode, the step-down mode, and the transition operation mode are presented. The proposed circuit architecture had a high voltage-conversion ratio and a simple architecture. A prototype bidirectional DC–DC converter with a full load of 500 W, a low side voltage of 24 V, and a high side voltage of 200 V was developed to prove the concept. The feasibility of the rapid energy bidirectional transition technology was verified by the simulation results and experimental results using the prototype converter. The maximum efficiencies in the step-up mode and the step-down mode were 95.3% and 93.8% respectively. Under full-load conditions, the transient time of the energy transition from the step-up mode to the step-down mode was 17.7 μ s, and the transient time of the energy transition from the step-down mode to the step-up mode was 19.3 μ s.

Keywords: bidirectional DC–DC converter; energy transition; commutation interval; energy storage system



Citation: Liao, H.; Chen, Y.-T.; Chen, L.; Chen, J.-F. Development of a Bidirectional DC–DC Converter with Rapid Energy Bidirectional Transition Technology. *Energies* **2022**, *15*, 4583. <https://doi.org/10.3390/en15134583>

Academic Editors: Vincenzo Di Dio and Valeria Boscaino

Received: 27 April 2022

Accepted: 20 June 2022

Published: 23 June 2022

Publisher's Note: MDPI stays neutral with regard to jurisdictional claims in published maps and institutional affiliations.



Copyright: © 2022 by the authors. Licensee MDPI, Basel, Switzerland. This article is an open access article distributed under the terms and conditions of the Creative Commons Attribution (CC BY) license (<https://creativecommons.org/licenses/by/4.0/>).

1. Introduction

With the advancement of technology, the dependence on electrical products for modern daily life has increased. To achieve the sustainable development of society and the economy, a balance between environmental protection and energy utilization has become increasingly important [1,2]. However, conventional electricity generation methods such as thermal power generation with fossil fuels or natural gas result in severe environmental pollution. To achieve sustainable power generation with minimal economic compromises and improved environmental protection, electricity generation using renewable energy has become one of the most popular choices.

Power generation with renewable energy such as solar power, wind power, and fuel cells has been widely used in the past decade [3–6]. The advantages of utilizing renewable energy for power generation include the renewability of the energy sources and low environmental pollution. However, due to the instability of the renewable energy sources, power generation with renewable energy is unstable and results in intermittent electricity formation. Therefore, the use of power electronic technology is required to improve the efficiency and stability of renewable energy conversion [7–11].

Moreover, a renewable energy system needs to provide enough energy to meet the load when the load demand increases. A change in load demand could introduce voltage sag and short interruptions during the conversion process [12,13]. Incidents such as motor shutdowns due to inverter voltage loss-protection actions, programmable logic controller (PLC) failures, and computer storage data loss are mainly caused by voltage sags [14]. Due to the concerned issues, rapid energy-conversion techniques have become very important for the power grid.

To reduce the transition voltage and current in the transition period, various converters are used to reduce the load current for a smooth power transfer in the system [15–19]. However, this method limits the power capacity during conversion. Figure 1 shows the typical renewable energy storage system in a DC microgrid [20]. A renewable-energy power-generation system is a type of distributed energy system with an energy storage system (ESS) as the backup power system. The functions of the ESS include the ability to handle the occurrence of intermittent outages for grid applications [21,22], the storage of the excess electricity generated from renewable energy resources, and the discharging of batteries stored when an insufficient energy supply occurs or during energy consumption's peak times [23–25]. Therefore, designing an efficient bidirectional DC–DC converter is critical in ESSs to achieve a better bidirectional power-flow capability [26]. In addition, in the process of energy conversion, maintaining a smooth power transfer is one of the important aspects. Therefore, enforcing a smooth power transfer in the bidirectional converter design is important in energy supply or energy-storage setups. This can be achieved by providing a sufficient voltage-conversion ratio for the energy conversion of the bidirectional DC–DC converter to improve the system's power quality [27]. In this study, a bidirectional DC–DC converter with a high voltage-conversion ratio based on rapid energy-conversion techniques was proposed. This converter can be utilized to achieve a fast bidirectional energy transfer between the battery of the ESS and the DC bus. The operational theory of the DC–DC bidirectional converter with rapid energy transition is presented in Section 3, along with the proposed implementation methods and feasibility verifications. New control schemes are also presented in this study for the proposed bidirectional DC–DC converters. The proposed bidirectional converter topology was used as an example experiment to verify the feasibility of the technique.

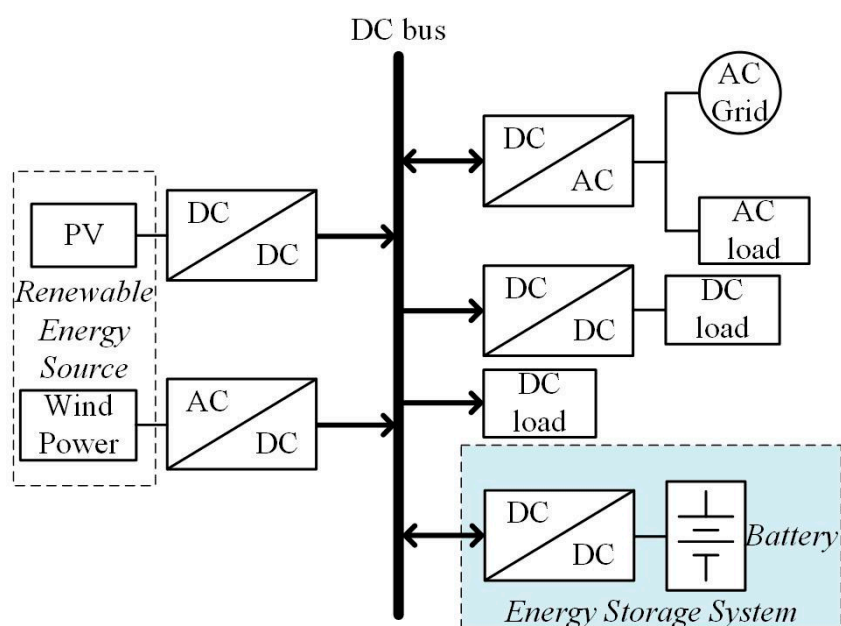


Figure 1. Energy storage system in DC microgrid.

2. Reviews of Bidirectional DC–DC Topologies

Bidirectional DC–DC converters are popular in industrial applications for managing renewable-energy power generation [28–31]. There are two common types of bidirectional converters available in the industry: the isolated bidirectional DC–DC converter and the nonisolated bidirectional DC–DC converter. The main difference is that the isolated converter can obtain a higher voltage ratio by adjusting the turn ratio of the designed transformers. On the other hand, the nonisolated bidirectional converter usually consists of either a cascade or cascode structure with a coupled-inductor or switched capacitor for a higher conversion output [32,33].

The single-stage bidirectional DC–DC converter is a commonly used circuit. The advantages of the single-stage DC–DC bidirectional converter include simple topologies and controlling methods, a low cost, and a high efficiency. To achieve the expected voltage gain, conventional bidirectional DC–DC converters are constructed by cascading or cascoding multiple single-stage converters [34,35]. In recent years, converters with topologies using coupled inductors and switched capacitors have become more popular. Although adjusting the turns ratio of the transformer can achieve a high conversion ratio, the leakage inductance of the coupled inductor and the parasitic capacitance of the main switch will resonate. This results in the occurrence of high voltage stress, and affects the efficiency of the whole circuit. In this situation, a resistor–capacitor–diode (RCD) snubber circuit can be used with a coupled-inductor DC–DC converter to reduce the main switch voltage spike and transfer the leakage inductance to the output.

Alternatively, adding the coupled-inductor and clamping circuits to the cascaded bidirectional DC–DC converter can also be an effective method [36]. The clamping switch can reduce the switching loss and improve the efficiency due to the zero-voltage switching characteristic. An example of a bidirectional half-bridge DC–DC converter with conventional buck and boost functions is shown in Figure 2 [37,38]. Although the circuit structure of the bidirectional half-bridge DC–DC converter is simple due to fewer switches being required in the structure, the voltage-conversion ratio is limited to the same level as the conventional buck and boost converters. This is due to the existence of parasitic resistance, which results in the difficulty in achieving a high conversion efficiency. To improve the voltage-conversion ratio, the tapping inductor needs to be changed or interleaved. There are some derived topologies for cascade or interleave converters that have been presented previously [39–41]. The single-stage cascaded bidirectional DC–DC converter constructed by cascading the described bidirectional half-bridge DC–DC converters based on this operational principle is shown in Figure 3 [42,43]. The cascaded bidirectional buck–boost/half-bridge DC–DC converter is shown in Figure 4 [39]. The two-phase interleaved cascaded bidirectional buck–boost/half-bridge DC–DC converter is shown in Figure 5 [40], and the interleaved bidirectional switched-boost DC–DC converter is shown in Figure 6 [41].

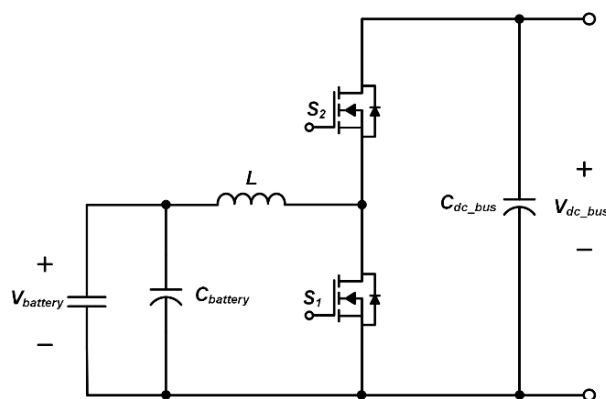


Figure 2. The topology of the half-bridge bidirectional DC–DC converter.

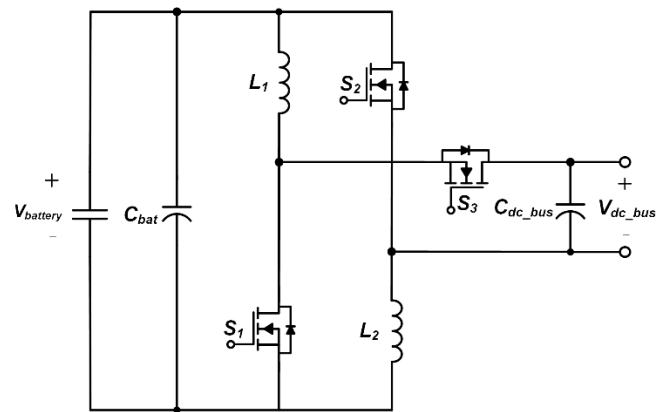


Figure 3. A single-stage bidirectional DC-DC converter.

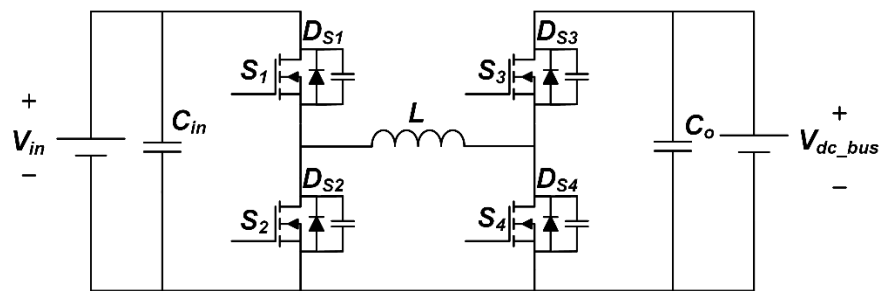


Figure 4. Cascaded bidirectional buck-boost/half-bridge DC-DC converter.

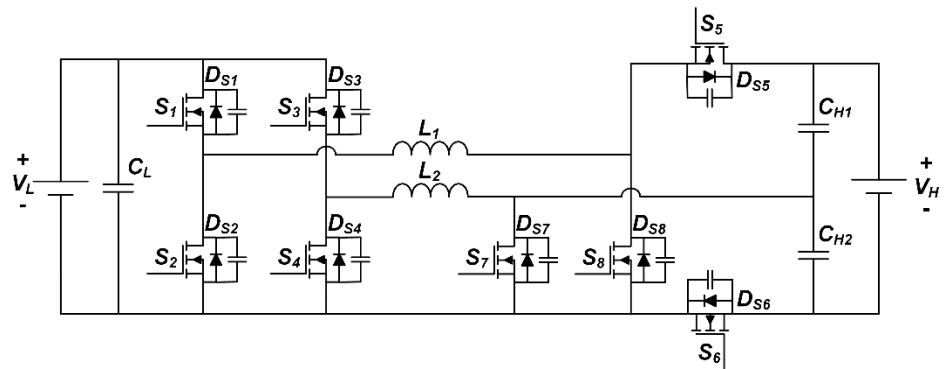


Figure 5. Two-phase interleaved cascaded bidirectional buck-boost/half-bridge DC-DC converter.

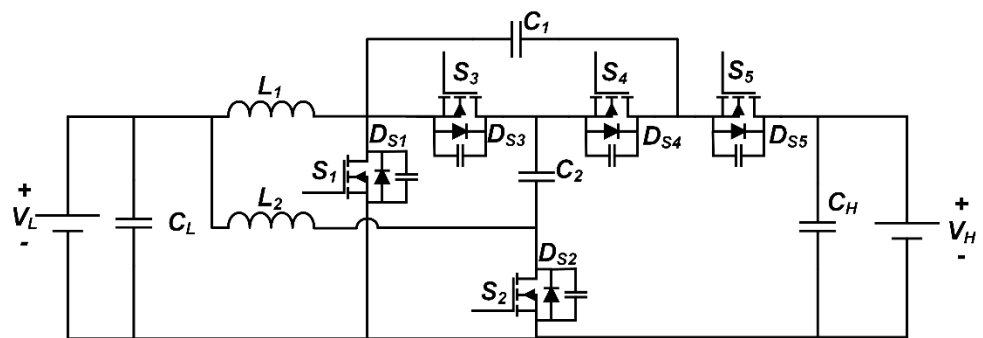


Figure 6. Interleaved bidirectional switched-boost DC-DC converter.

In general, the bidirectional converter uses the main switch for energy transfer, and the remaining switches are turned off as rectifier diodes. If the energy needs to be transferred in the reverse direction, the function of the switch can be exchanged. The isolationrconverter

usually uses the transformer turns ratio to achieve a high voltage-conversion ratio. However, the leakage inductance of the transformer can cause additional loss and damage to the switching element. In the nonisolated converter, the voltage-conversion ratio of the conventional single-stage converter is limited by parasitic components. The voltage-conversion ratio can only be improved by combining multiple single-stage converters through the cascade, series, stack, or coupled-inductor techniques.

A comparison of the voltage-conversion ratios of the nonisolated bidirectional DC–DC converters described above is shown in Figure 7 [39–43]. Figure 7a shows the voltage-conversion ratio in the step-up mode, and Figure 7b is the voltage-conversion ratio in the step-down mode. As shown in Figure 7, the highest voltage-conversion ratio was achieved by the interleaved bidirectional switched-boost DC–DC converter with a complicated circuit architecture [41]. Therefore, based on the comparisons shown in Figure 7, the single-stage cascaded bidirectional DC/DC converter with a simpler circuit structure and relatively high voltage-conversion ratio [43] was used as the principle circuit architecture for this research.

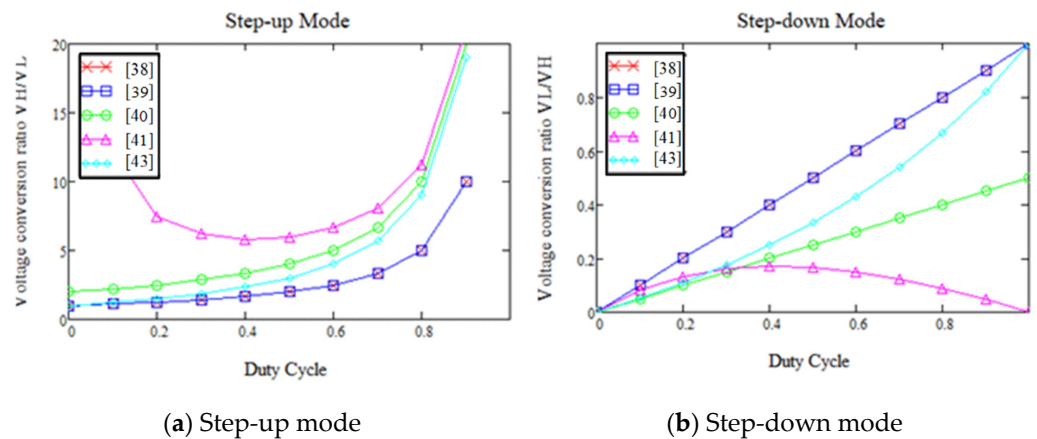


Figure 7. Comparison of voltage-conversion ratios of nonisolated bidirectional DC–DC converters [38–41,43].

The circuit architecture presented in Figure 3 was used as the main circuit structure for the proposed conversion strategy. An LC resonate circuit with rapid energy bidirectional transition technology was applied to this architecture; the new bidirectional DC–DC converter topology is shown in Figure 8. To minimize the load fluctuations, the transition time of the changes in the converter power flow was shortened using the transition technology described in detail below.

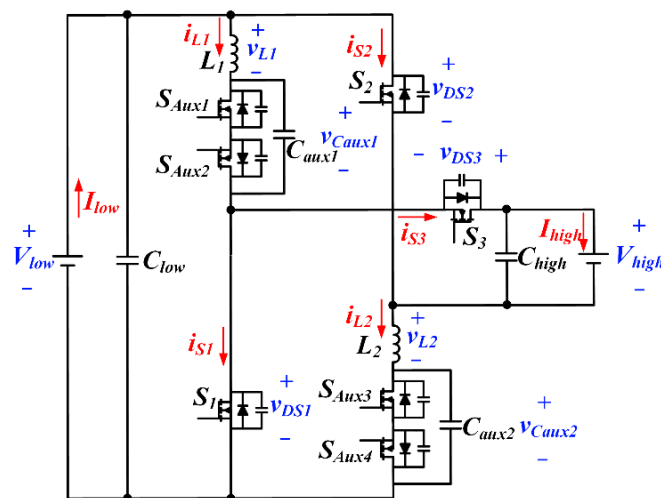


Figure 8. Circuit topology of the proposed bidirectional DC–DC converter.

3. Technique and Control Strategy of Rapid Energy Conversion

To reduce the size and improve the efficiency and other factors, single-stage bidirectional DC–DC converters are widely used. The bidirectional DC–DC converters that use the new conversion techniques can be applied in distributed systems and ESSs of the microgrid systems for power-flow stabilization [21–25]. The reduction in the converter’s conversion efficiency, which is caused by the instability of the power flow, can be minimized when the battery modules are connected to the DC bus [14–16]. The duration for changing the power flow of a bidirectional DC–DC converter needs to be minimized. This indicates that the transition status needs to be closely monitored when the operation mode is changed. The length of the transition time influences the power flow and causes load fluctuations [44–47]. This research proposed alternative transfer methods of rapid energy bidirectional conversion that could minimize the transition time of the converter’s power-flow change. The definition of the transition time in this paper was divided into two different types: the transient time—the time for the converter to reach the required reverse power from the required original power; and the settling time—the time for the converter’s power to reach the final required power after the power transition. The errors of the entire transition process can be maintained within a certain range ($\pm 10\%$).

Figure 9 shows the circuit diagram of a bidirectional DC–DC converter with rapid energy conversion. There are two main functions in the circuit: the step-up mode and the step-down mode. The design and calculation of the energy-conversion control must include the consideration of the direction of the inductor current or capacitor voltage. If a sudden change in the direction occurs, the inductor current or the voltage in the capacitor could cause damage to the power components in the circuit. This section explains the methods used for performing the rapid energy conversion under the same specification of the applied converter. The architecture of the single-stage bidirectional DC–DC converter in Figure 3 was used in this study for the analyses of the step-up mode and step-down mode given in Section 2. In the two operation modes, a section of current or voltage with inductance or capacitance in the same state was selected to perform the rapid energy conversion.

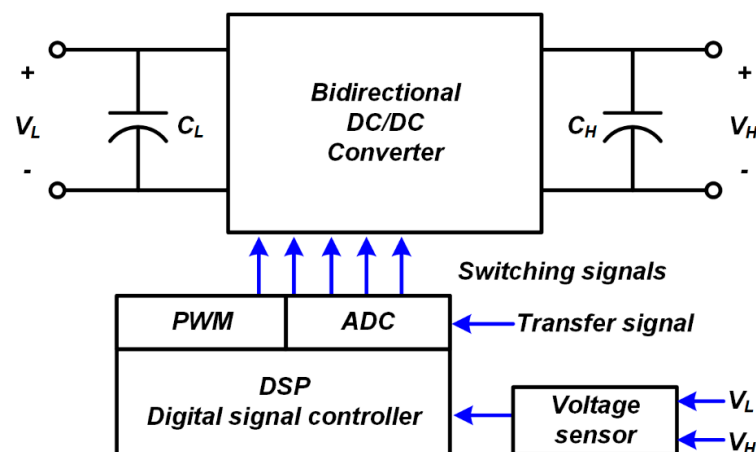


Figure 9. A bidirectional circuit diagram of rapid energy conversion.

3.1. Transition Operation Mode Analysis

Z. Chen et al. presented an energy-conversion concept in a bidirectional DC–DC converter [48]. However, the transition period could not be balanced in two operation modes. In this research, a bidirectional DC–DC converter with an LC path could achieve a balanced transition time in two operation modes in continuous conduction mode (CCM). The circuit topology of the proposed bidirectional DC–DC converter circuit in this study is shown in Figure 5. The circuit was composed of seven power switches ($S_1, S_2, S_3, S_{aux1}, S_{aux2}, S_{aux3}, S_{aux4}$), two inductors (L_1, L_2), and four capacitors ($C_{low}, C_{high}, C_{aux1}, C_{aux2}$). $S_{aux1}, S_{aux2}, S_{aux3}, S_{aux4}, C_{aux1}$, and C_{aux2} were used to achieve rapid energy bidirectional transition.

To simplify the topology analysis, several assumptions were made:

- (a) The capacitance of C_{low} and C_{high} were large enough to make the voltage across the capacitor constant.
- (b) The body diodes of all power switches were considered.
- (c) All components were ideal, and the impact of the dead time of the driving signal was ignored.

It was necessary to consider the direction of the energy storage element in the circuit during the power-flow transition period of the bidirectional converter. An instantaneous change in the direction of the inductor current and capacitor voltage should be avoided to prevent a sudden rise in the changing rate of current and voltage, which can cause a surge in the circuit and damage switching components. Adding a resonance path in the circuit architecture can prevent a surge in the circuit during the energy transition.

3.1.1. Transition from Step-Up Mode to Step-Down Mode

In the transient interval of the transition from step-up mode to step-down mode, since the operation of the switch in the step-up discharging mode and the step-down charging mode were the same, the transition could be performed based on this. A key waveform diagram of the transition from the step-up mode to the step-down mode showing the process of the transient interval of transition is shown in Figure 10.

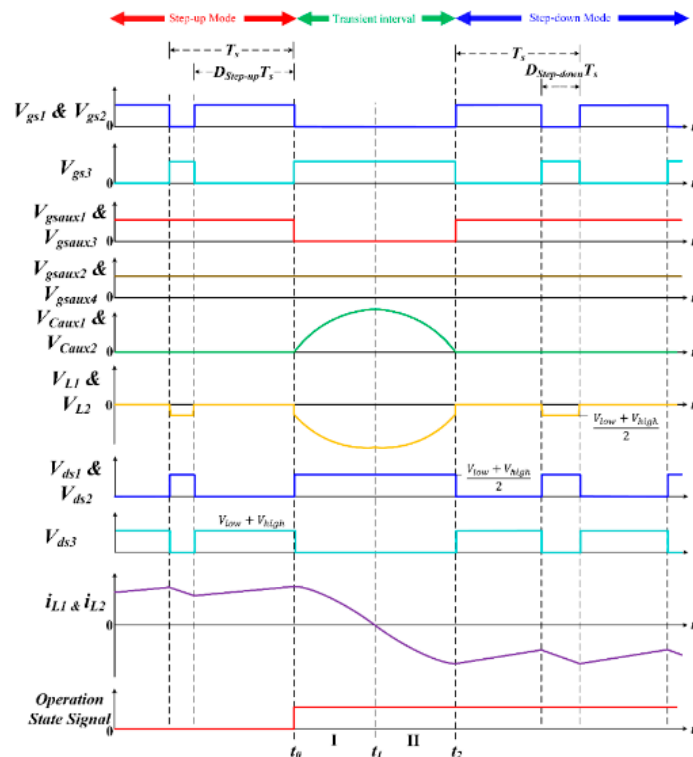


Figure 10. The process of the transition from the step-up mode to the step-down mode.

The circuit would operate in the step-up mode if the operation state signal change was not received. The duty cycle of the main switches S_1 and S_2 was labeled as $D_{Step-up}$. The power switches (S_{aux1} , S_{aux2} , S_{aux3} , and S_{aux4}) remained on, and the auxiliary capacitors (C_{aux1} and C_{aux2}) did not join the circuit operation. Once the operation state signal change was received, the circuit began to enter the transient interval of the transition interval.

Step-Up Mode to Step-Down Mode I (t_0-t_1)

When the change of the operation state signal was detected, the circuit entered the transient interval of transition. The main switches S_1 and S_2 turned off, while S_3 turned on. The auxiliary switches (S_{aux1} and S_{aux3}) also turned off. The auxiliary capacitors (C_{aux1} and C_{aux2}) joined the circuit operation and resonated with the inductors (L_1 and L_2). The

inductor currents (i_{L1} and i_{L2}) began to decrease, and the auxiliary capacitors (C_{aux1} and C_{aux2}) began to store energy until the inductor currents (i_{L1} and i_{L2}) decreased to zero. The current path is shown in Figure 11a.

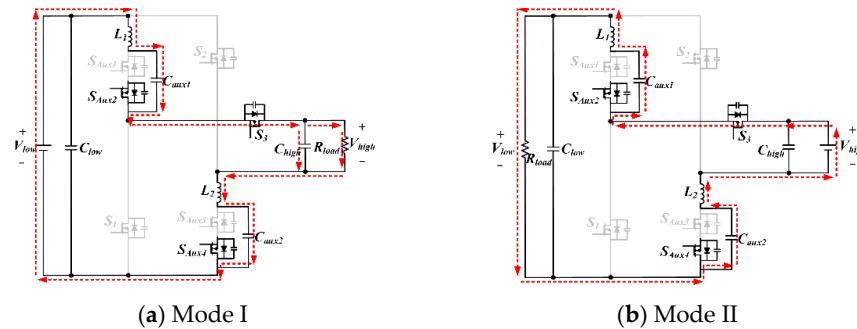


Figure 11. The current flow path of transition from step-up mode to step-down mode.

Step-Up Mode to Step-Down Mode II (t_1-t_2)

At $t = t_1$, the inductor currents (i_{L1} and i_{L2}) decreased to zero. The auxiliary capacitors (C_{aux1} and C_{aux2}) discharged, and the inductors (L_1 and L_2) began to store energy in the opposite direction. When the auxiliary capacitor voltages ($v_{C_{aux1}}$ and $v_{C_{aux2}}$) decreased to zero, the body diodes of the auxiliary switches (S_{aux1} and S_{aux3}) turned on. The current path is shown in Figure 11b. The circuit left the transient interval of transition; when it did so, the circuit operated in the step-down mode. The main switch became S_3 , and the duty cycle was $D_{Step-down}$. The auxiliary switches (S_{aux1} , S_{aux2} , S_{aux3} , S_{aux4}) remained on. The auxiliary capacitors (C_{aux1} and C_{aux2}) did not join the circuit operation.

3.1.2. Transition from Step-Down Mode to Step-Up Mode

In the transient interval of the transition from step-down mode to step-up mode, since the operation of the switch in the step-down discharging mode and the step-up charging mode were the same, the transition could be performed based on this. A key waveform diagram of the transition from the step-down mode to the step-up mode showing the process of the transient interval of transition is shown in Figure 12.

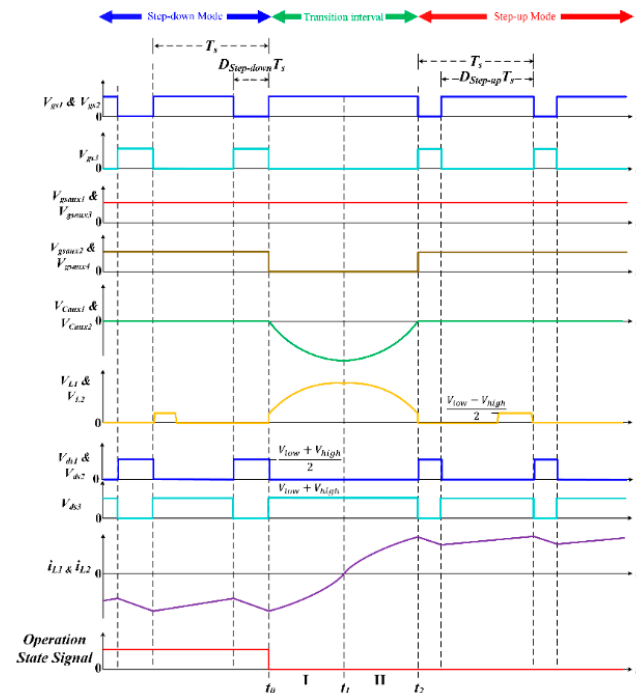


Figure 12. The process of the transition from the step-down mode to the step-up mode.

The circuit would operate in the step-down mode if the operation-state signal change was not detected. The duty cycle of the main switch S_3 was $D_{Step-down}$. The power switches (S_{aux1} , S_{aux2} , S_{aux3} , S_{aux4}) remained on, and the auxiliary capacitors (C_{aux1} and C_{aux2}) did not join the circuit operation. Once the operation-state signal change was detected, the circuit began to enter the transient interval of the transition.

Step-Down to Step-Up Mode I (t_0-t_1)

When the change of the operation state signal was received, the circuit entered the transient interval of transition. The main switch S_3 turned off, while S_1 and S_2 turned on. The auxiliary switches (S_{aux2} and S_{aux4}) also turned off. The auxiliary capacitors (C_{aux1} and C_{aux2}) joined the circuit operation and resonated with the inductors (L_1 and L_2). The reverse inductor currents (i_{L1} and i_{L2}) began to decrease, and the auxiliary capacitors (C_{aux1} and C_{aux2}) began to store energy in the opposite direction until the reverse inductor currents (i_{L1} and i_{L2}) decreased to zero. The current path is shown in Figure 13a.

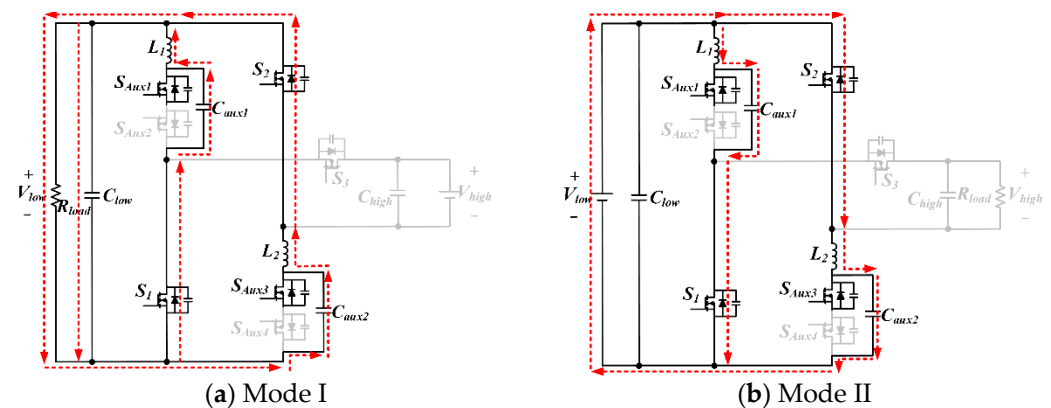


Figure 13. The current flow path of transition from step-down to step-up mode.

Step-Down to Step-Up Mode II (t_1-t_2)

At $t = t_1$, the reverse inductor currents (i_{L1} and i_{L2}) decreased to zero. The auxiliary capacitors (C_{aux1} and C_{aux2}) discharged, and the inductors (L_1 and L_2) began to store energy in the positive direction. When the reverse auxiliary capacitor voltages (v_{Caux1} and v_{Caux2}) decreased to zero, the body diodes of the auxiliary switches (S_{aux2} and S_{aux4}) turned on. The current path is shown in Figure 13b. The circuit exited the transient interval of transition; when it did so, the circuit operated in the step-up mode. The main switches became S_1 and S_2 , and the duty cycle was $D_{Step-up}$. The auxiliary switches (S_{aux1} , S_{aux2} , S_{aux3} , S_{aux4}) remained on, and the auxiliary capacitors (C_{aux1} and C_{aux2}) did not join the circuit operation.

3.2. Transition Control Strategy

The control strategy is particularly important in the energy bidirectional transition. To prevent the surge caused by a sudden change in the direction of the energy-storage element in the circuit, it is necessary to formulate a control strategy and use a digital signal processor (DSP) in conjunction with the control strategy in the circuit operation during the transition interval.

The circuit determined whether to start the bidirectional energy transition according to the change in the operation-state signal. If the circuit had not received the operation-state signal change, it would operate according to the present operation-state signal. If the operation-state signal was set at high, the circuit operated in the step-down mode. On the contrary, if the operation state signal was set at low, the circuit operated in the step-up mode.

If the circuit received a change in the operation-state signal, it would determine whether the operation state signal was an upper-edge or a lower-edge trigger first, then operated according to different trigger conditions for the power flow of the circuit to achieve the transition. If the operation state signal was triggered by the upper edge, the

converter transitioned from the step-up mode to the step-down mode. On the contrary, if it was triggered by the lower edge, the converter transitioned from the step-down mode to the step-up mode.

3.3. Component Parameter Design on Transient Interval

The equivalent circuit for the transient interval from step-up mode to step-down mode is shown in Figure 14. The auxiliary capacitors (C_{aux1} and C_{aux2}) were added to the circuit to resonate with the inductors (L_1 and L_2) to speed up the energy-direction conversion. The transient time depended on the values of the auxiliary capacitors (C_{aux1} and $298 C_{aux2}$). Therefore, determining the values of the capacitors to minimize the transient time required for the mode transition was one of the crucial aspects of this design.

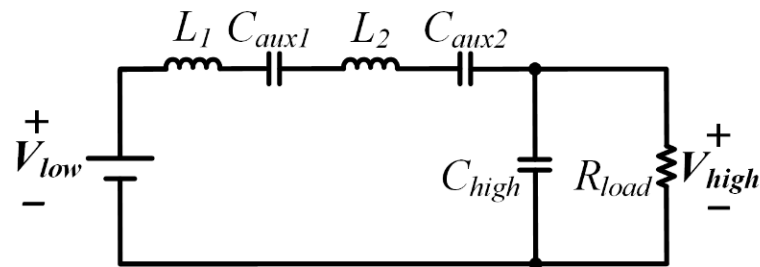


Figure 14. The equivalent circuit from step-up mode to step-down mode.

The Laplace equivalent circuit for the mode transition is shown in Figure 15, where L_s is the equivalent inductance of L_1 and L_2 in series, $i_{L_s}(0)$ is the initial value of the series inductor L_s , $V_{C_{high}}(0)$ is the initial voltage across the capacitor C_{high} at the high-voltage side, and R_{load} is the load in the step-up mode.

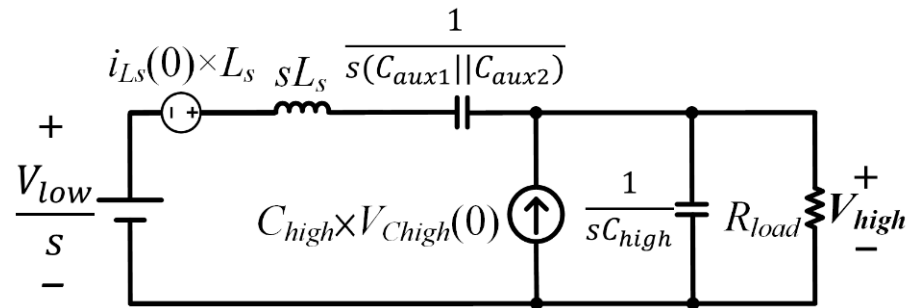


Figure 15. The Laplace equivalent circuit from step-up mode to step-down mode.

The equivalent equation of the auxiliary capacitor voltage $v_{C_{aux1}}$ is shown in Equation (1):

$$v_{caux1}(s) = \frac{\frac{v_{low}}{s} + i_{L_s}(0) \times L_s - C_{high}(0) \times \frac{\frac{1}{sC_{high}} \times R_{load}}{\frac{1}{sC_{high}} + R_{load}}}{s \times L_s + \frac{1}{s(C_{aux1} || C_{aux2})} + \frac{\frac{1}{sC_{high}} \times R_{load}}{\frac{1}{sC_{high}} + R_{load}}} \times \frac{1}{sC_{aux1}}. \tag{1}$$

The initial values of the inductors (L_1 and L_2) and the output capacitor C_{high} were converted by Laplace. The Laplace equivalent circuit of the transition from step-down to step-up mode is shown in Figure 16, where $i_{L1}(0)$ is the initial value of the inductor L_1 , $i_{L2}(0)$ is the initial value of the inductor L_2 , $V_{C_{low}}(0)$ is the initial voltage across the capacitor C_{low} at the low-voltage side, and R_{load} is the load in the step-down mode.

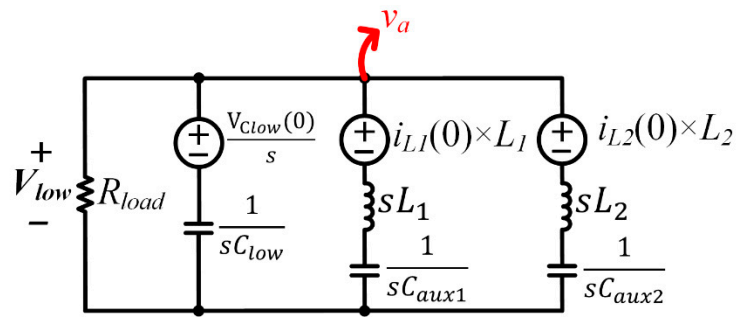


Figure 16. The Laplace equivalent circuit from step-down mode to step-up mode.

Using the Laplace equivalent circuit and the node-voltage method, the equation for the node voltage v_a is shown in Equation (2):

$$\frac{v_a}{R_{load}} + \frac{v_a - \frac{v_{clow}(0)}{s}}{\frac{1}{sC_{low}}} + \frac{v_a - i_{L1}(0) \times L_1}{sL_1 + \frac{1}{sC_{aux1}}} + \frac{v_a - i_{L2}(0) \times L_2}{sL_2 + \frac{1}{sC_{aux2}}} = 0. \tag{2}$$

Since the inductance of L_1 and L_2 were equal, the initial inductor currents across L_1 and L_2 were also the same. By solving v_a , the equivalent equation of the reverse auxiliary capacitor voltage v_{Caux1} can be derived from Equation (3):

$$v_{caux1}(s) = \frac{v_a - i_{L1}(0) \times L_1}{sL_1 + \frac{1}{sC_{aux1}}} \times \frac{1}{sC_{aux1}}. \tag{3}$$

The voltage across the auxiliary capacitor and the relationship between the capacitance of the auxiliary capacitor and the transient time of the mode transition in the reverse direction could be obtained by inverse Laplace transformation of Equation (3). The auxiliary capacitor value was selected as 220 nF for this example experiment.

3.4. Component Design of Transition Technology

According to the inverse Laplace transformation of Equations (1) and (3), the relationship between the auxiliary capacitor and the voltage across the auxiliary capacitor could be obtained. As illustrated in Figure 17, the curve showed the transition time and the voltage across the auxiliary capacitor with different capacitor values.

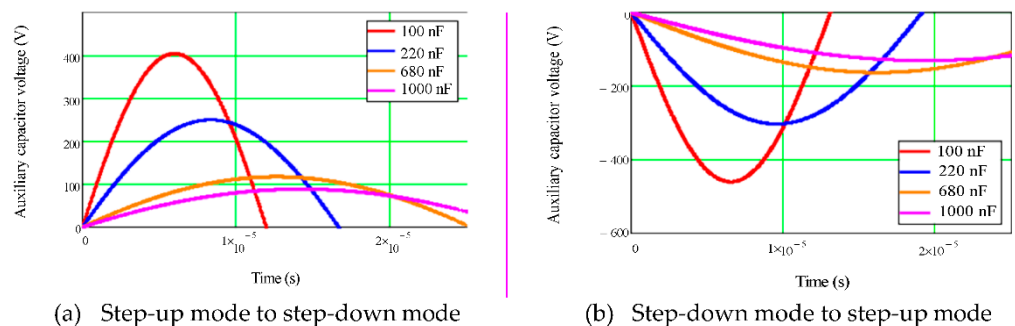


Figure 17. The transition time curve with different auxiliary capacitor values under the full-load condition.

It should be noted that since the transition control strategy would cause the voltage across the auxiliary capacitor to be clamped to zero when it changed to the opposite direction, only the positive half cycle in the curve needed to be analyzed. The transition time curve from the step-up mode to the step-down mode is shown in Figure 17a, and the transition time curve from the step-down mode to the step-up mode is shown in Figure 17b.

According to the results shown in Figure 17, to limit the transient time of the transition within one switching cycle ($20 \mu\text{s}$), the auxiliary capacitor value had to be less than 220 nF . Therefore, the value of the auxiliary capacitor was 220 nF for this analysis.

4. Experimental Results

The example experiment used the resonant transfer method. The system specification is shown in Table 1. The component parameters used in the experimental circuit are shown in Table 2. The hardware circuit diagram of the proposed converter is shown in Figure 18. The circuit was constructed with seven power switches, two inductors, and eight capacitors. A digital signal processor (DSP) was used to generate the PWM signal and for rapid energy bidirectional transition control.

Table 1. Specifications of the experimental system.

Step-Up Mode		Step-Down Mode	
Low-side voltage, V_{low}	24 V	High-side voltage, V_{high}	200 V
High-side voltage, V_{high}	200 V	Low-side voltage, V_{low}	24 V
Output power, P_{set-up}	500 W	Output power, $P_{set-down}$	500 W
Switching frequency, f_s	50 kHz	Switching frequency, f_{s2}	50 kHz

Table 2. Parameters of the experimental system.

Item	Value
Inductors L_1, L_2	185 μH
Capacitor C_{low}	35 $\mu\text{F}/35 \text{ V}$
Capacitor C_{high}	22 $\mu\text{F}/250 \text{ V}$
Auxiliary capacitor C_{aux1}, C_{aux2}	220 nF/600 V
Main switches S_1, S_2, S_3	IMW65R048M1H (650 V/39 A/48 m Ω)
Auxiliary switches $S_{Aux1}, S_{Aux2}, S_{Aux3}, S_{Aux4}$	SCTWA90N65G2V-4 (650 V/119 A/24 m Ω)
Digital signal processor (DSP)	TMS320F28379D

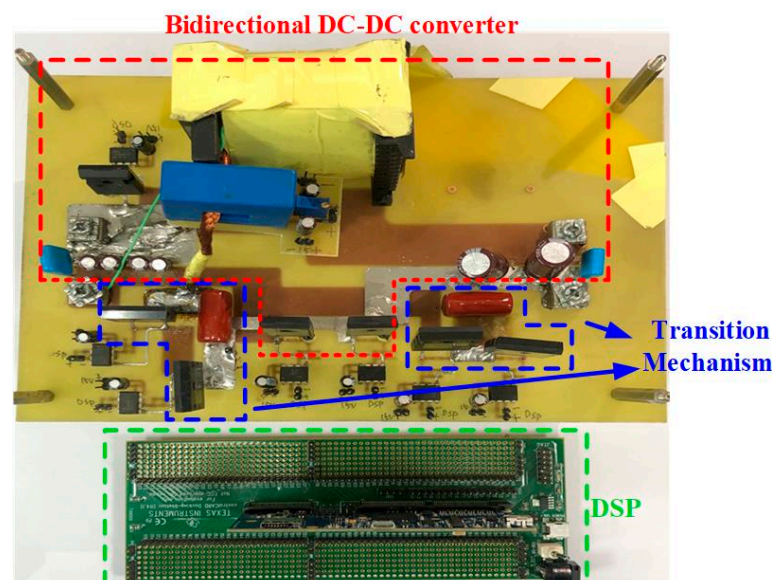


Figure 18. Image of the example experimental circuit.

4.1. Step-Up Mode to Step-Down Mode in CCM Stage

The experimental waveform of the transition from step-up mode to step-down mode with the half-load condition is shown in Figure 19. The measured waveforms could be classified into three modes: step-up mode, step-down mode, and commutation interval. The circuit initially operated in the step-up mode with the auxiliary switches (S_{aux1} and

S_{aux3}) turned on. When the operation state signal was changed from low to high, the circuit entered the transition interval. During the transition interval, the auxiliary switches (S_{aux1} and S_{aux3}) turned off, and the auxiliary capacitors (C_{aux1} and C_{aux2}) were added to the circuit for operation. The inductors (L_1 and L_2) and the auxiliary capacitors (C_{aux1} and C_{aux2}) began to resonate. When the inductor current changed to the negative direction and the voltage across the auxiliary capacitor was clamped at zero, the transition was completed. The circuit left the transient interval and began operation in step-down mode. In addition, due to the existence of a slight delay in the digital signal processor (DSP)'s processing signals, the signals did not act immediately upon entering and leaving the transient interval. Despite this, the transient time of the transition was still achieved within one switching cycle at 15.4 μs .

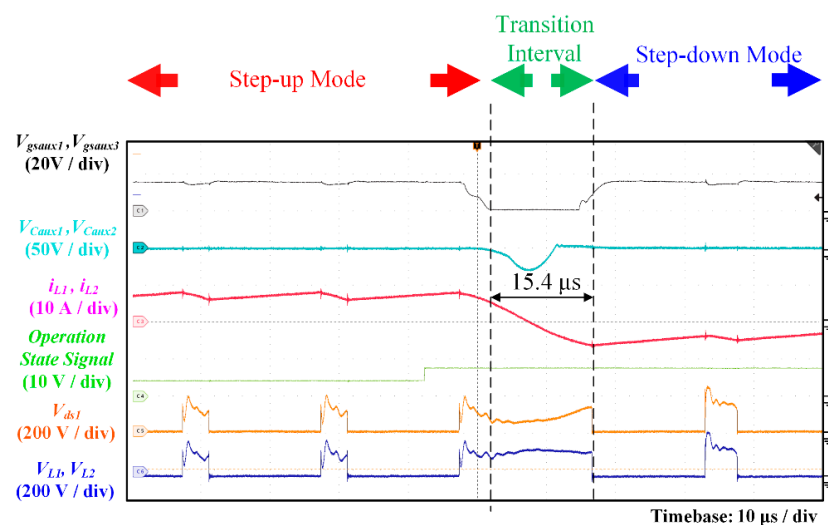


Figure 19. Experimental waveforms of transition from step-up mode to step-down mode with a half-load condition.

The experimental waveform of the transition from step-up mode to step-down mode with a full-load condition is shown in Figure 20. The transient time of the transition was within one switching cycle at 17.7 μs . The transient time of the transition at full load was longer than at half-load due to the different initial values of the inductor current. The initial value of the inductor current at full load was larger, and hence had a longer transient time.

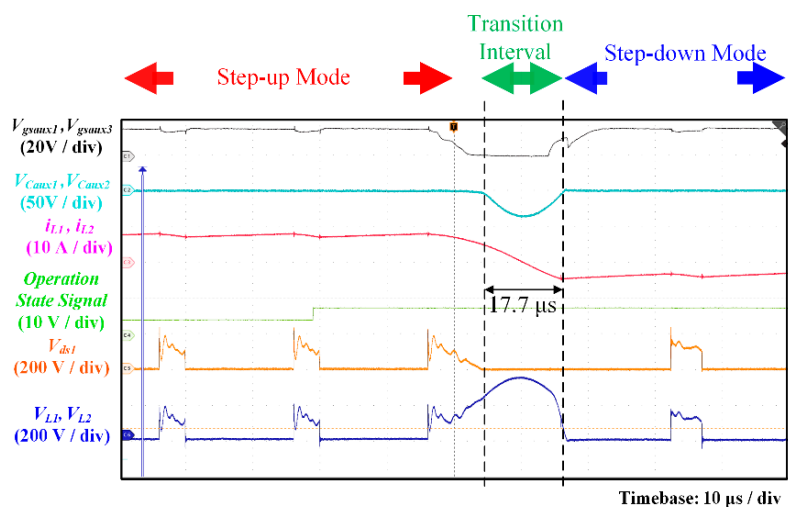


Figure 20. Experimental waveforms of transition from step-up mode to step-down mode under full-load conditions.

4.2. Step-Down Mode to Step-Up Mode in CCM

The experimental waveform of the transition from step-down mode to step-up mode under the half-load condition is shown in Figure 21. The circuit initially operated in the step-down mode, and the auxiliary switches (S_{aux2} and S_{aux4}) were on. When the operation state signal changed from high to low, the circuit entered the transient interval of the transition. During the transient interval, the auxiliary switches (S_{aux2} and S_{aux4}) were off, and the auxiliary capacitors (C_{aux1} and C_{aux2}) were added to the circuit for operation. The inductors (L_1 and L_2) and the auxiliary capacitors (C_{aux1} and C_{aux2}) began to resonate. When the inductor current changed to the positive direction and the voltage across the auxiliary capacitor was clamped at zero, the transition was completed. The circuit left the transient interval and began operation in step-up mode. In addition, due to the existence of a slight delay in the digital signal processor (DSP)'s processing signals, the signals would not act immediately upon entering or leaving the transient interval. Despite this, the transient time of the transition was still achieved within one switching cycle at 18.6 μs .

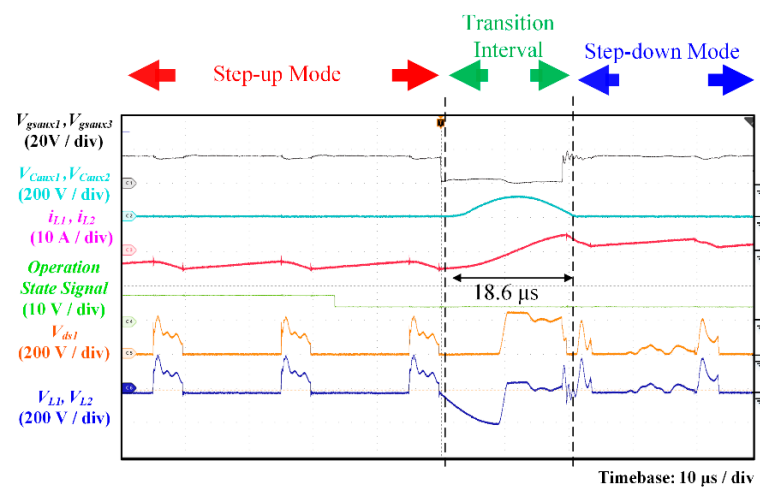


Figure 21. Experimental waveforms of transition from step-down mode to step-up mode under the half-load condition.

The experimental waveform of the transition from step-down mode to step-up mode under the full-load condition is shown in Figure 22. The transient time of the transition was within one switching cycle at 19.3 μs . The transient time of the transition at full load was longer than at half-load due to the different initial values of the inductor current. The initial value of the inductor current at full load was larger, and hence had a longer transient time.

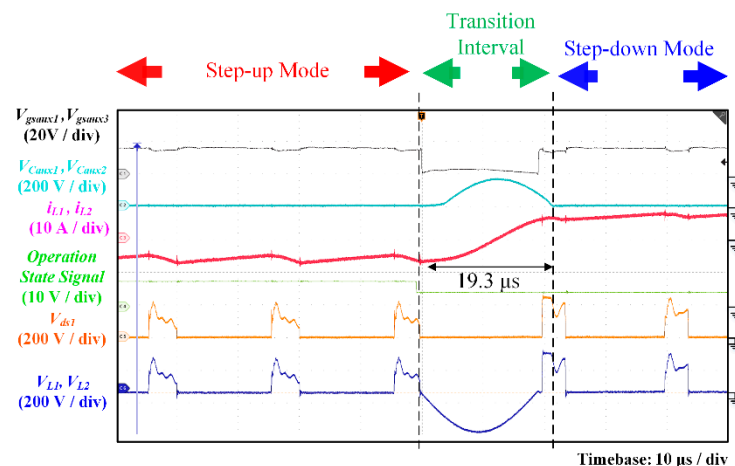


Figure 22. Experimental waveforms of transition from step-down mode to step-up mode under the full-load condition.

By comparing the simulation waveforms in Figures 19–22, the simulation results were found to be consistent with the experimental results. The feasibility of rapid energy bidirectional transition technology was verified. Since the power flow could not be measured in the experiment, the power-flow transition was indirectly verified using the waveform of the inductor current.

Some previous publications briefly mentioned the transient time; however, the specification of transient time was not discussed in detail. The transition time discussed in our previous work was around 15.4 μs to 19.3 μs during the CCM stage [48]. Three different stages (DCM, BCM, and CCM) were discussed in the previous work. The transient time from the step-up to the step-down mode in the CCM stage was 15.8 μs , but from step-down to the step-up mode in the CCM stage was 50.01 μs . Overall, the proposed method with the LC resonance path could balance the transition time in two modes. Therefore, the proposed conversion technique in this study was better than that in the previous work due to the shorter sum of transient times.

4.2.1. Efficiency in Step-Up Mode

The efficiency curve of the step-up mode with different loads is shown in Figure 23. The measurement result shows that the maximum efficiency reached 95.3% at 40% load, and the full-load efficiency reached 91.2%.

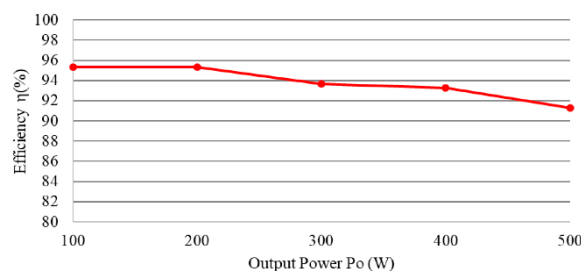


Figure 23. Efficiency curve in step-up mode.

4.2.2. Efficiency in Step-Down Mode

The efficiency curve of the step-down mode with different loads is shown in Figure 24. The measurement result shows that the maximum efficiency reached 93.8% at 60% load, and the full-load efficiency reached 92.0%.

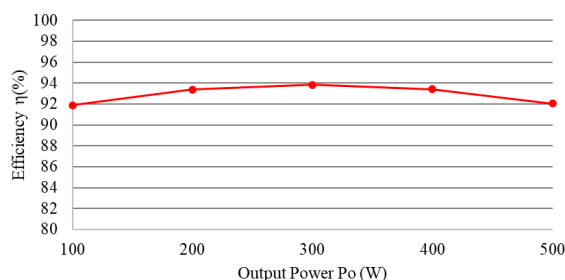


Figure 24. Efficiency curve in step-down mode.

4.2.3. Calculated Loss Distribution

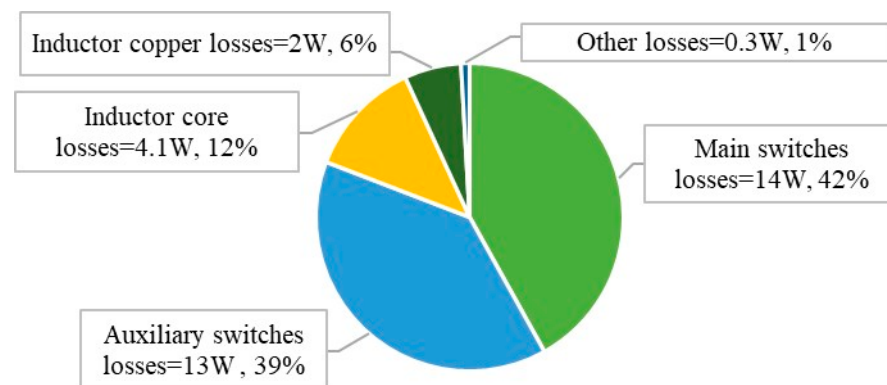
This converter power loss was roughly divided into three parts, including power loss in the main switches, auxiliary switches, and magnetic elements. The main-switch power losses included the switching loss and the conduction loss. Only the conduction loss was considered for the auxiliary-switch losses. This was because the auxiliary switches were on in both the step-up mode and the step-down mode. The magnetic element losses were the core loss and copper loss of the two inductors. The equations to derive the power losses in the main components are shown in Table 3.

Table 3. Equations to derive the power losses in main components.

Item	Equation
S_1	$\frac{v_{DS1} \times i_{S1}}{6} (t_{on} + t_{off}) \times f_s + i_{S1}^2 \times R_{ds(on)} \times \frac{T_{on}}{T}$
S_2	$\frac{v_{DS1} \times i_{S2}}{6} (t_{on} + t_{off}) \times f_s + i_{S2}^2 \times R_{ds(on)} \times \frac{T_{on}}{T}$
S_3	$\frac{v_{DS1} \times i_{S3}}{6} (t_{on} + t_{off}) \times f_s + i_{S3}^2 \times R_{ds(on)} \times \frac{T_{on}}{T}$
S_{aux1} & S_{aux2} & S_{aux3} & S_{aux4}	$i_{L,rms}^2 \times R_{ds(on)}$
L_1 & L_2	$(P_h + P_e) + i_{L,rms}^2 \times R_s$

P_h : hysteresis loss; P_e , eddy-current loss.

The calculated loss distribution under the full-load condition is shown in Figure 25.

**Figure 25.** Calculated loss distribution.

Due to the addition of the transition mechanism and the auxiliary switches always being on in both the step-up mode and the step-down mode, the conduction losses of the auxiliary switches accounted for a larger proportion of the loss. The losses of the auxiliary switches were 13 W, which reduced the efficiency of the converter by 2.6%.

5. Conclusions

This study proposed a rapid energy-transition conversion technique for a high voltage-conversion ratio bidirectional DC–DC converter between step-up and step-down mode. To overcome the already-known power flow issue, the proposed method could be applied to the energy conversion between the DC bus and the battery. It was essential to consider the direction of the inductor current or the capacitor voltage for energy-conversion control. A rapid conversion technique based on the resonant concept to transfer energy was proposed and analyzed in this paper. Despite advantages such as the high voltage-conversion ratio and simple structure of the proposed converter, an isolated driver circuit was required to drive the switches due to the battery side and the DC bus side not being connected to the common ground.

The experimental circuits were constructed to confirm the feasibility of the theoretical analyses. A bidirectional DC–DC converter with a low-side voltage of 24 V, a high-side voltage of 200 V, a rated output power of 500 W, and rapid energy bidirectional transition technology was implemented. The experimental results presented validated the effectiveness and the accuracy of the proposed control strategies and rapid energy conversion. The maximum efficiency in the step-up mode was 95.3%, and the maximum efficiency in the step-down mode was 93.8%. Applying the rapid energy bidirectional transition technology in full-load conditions resulted in a short transient time (17.7 μ s) of the transition from step-up mode to step-down mode. The transient time of the transition from step-down mode to step-up mode was also reduced to 19.3 μ s.

The transient time in this research could be achieved within one switching cycle. The experimental results verified that the application of the proposed conversion technique

provided an effective, safe, and rapid energy bidirectional transition regardless of the load conditions.

Author Contributions: Conceptualization, J.-F.C.; methodology, Y.-T.C.; software, Hsuan Liao; validation, Y.-T.C.; writing—original draft preparation, H.L.; writing—review and editing, L.C.; Project administration, J.-F.C. All authors have read and agreed to the published version of the manuscript.

Funding: This study was supported by the Delta Electronics Foundation, and it was financially supported by the Hierarchical Green-Energy Materials (Hi-GEM) Research Center, part of the Featured Areas Research Center Program within the framework of the Higher Education Sprout Project by the Ministry of Education (MOE) in Taiwan, as well as the Ministry of Science and Technology under the projects MOST 110-2221-E-006-125 and MOST 110-2634-F-006-017.

Conflicts of Interest: The authors declare no conflict of interest.

References

1. Al-Shetwi, A.Q.; Hannan, M.A.; Abdullah, M.A.; Rahman, M.S.A.; Ker, P.J.; Alkahtani, A.A.; Mahlia, T.M.I.; Muttaqi, K.M. Utilization of Renewable Energy for Power Sector in Yemen: Current Status and Potential Capabilities. *IEEE Access* **2021**, *9*, 79278–79292. [[CrossRef](#)]
2. Wu, C.; Zhang, X.-P.; Sterling, M.J.H. Economic Analysis of Power Grid Interconnections among Europe, North-East Asia, and North America with 100% Renewable Energy Generation. *IEEE Open Access J. Power Energy* **2021**, *8*, 268–280. [[CrossRef](#)]
3. Elavarasan, R.M.; Shafiullah, G.M.; Padmanaban, S.; Kumar, N.M.; Annam, A.; Vetrichevan, A.M.; Mihet-Popa, L.; Holm-Nielsen, J.B. A Comprehensive Review on Renewable Energy Development, Challenges, and Policies of Leading Indian States with an International Perspective. *IEEE Access* **2020**, *8*, 74432–74457. [[CrossRef](#)]
4. Ahmed, S.D.; Al-Ismail, F.S.M.; Shafiullah, M.; Al-Sulaiman, F.A.; El-Amin, I.M. Grid Integration Challenges of Wind Energy: A Review. *IEEE Access* **2020**, *8*, 10857–10878. [[CrossRef](#)]
5. Shafiullah, M.; Ahmed, S.D.; Al-Sulaiman, F.A. Grid Integration Challenges and Solution Strategies for Solar PV Systems: A Review. *IEEE Access* **2022**, *10*, 52233–52257. [[CrossRef](#)]
6. Tang, Z.; Yang, Y.; Blaabjerg, F. Power electronics: The enabling technology for renewable energy integration. *CSEE J. Power Energy Syst.* **2022**, *8*, 39–52.
7. Lu, X.; Guerrero, J.M.; Sun, K.; Vasquez, J.C. An improved droop control method for dc microgrids based on low band-width communication with dc bus voltage restoration and enhanced current sharing accuracy. *IEEE Trans. Power Electron.* **2014**, *29*, 1800–1812. [[CrossRef](#)]
8. Khorsandi, A.; Ashourloo, M.; Mokhtari, H. A Decentralized Control Method for a Low-Voltage DC Microgrid. *IEEE Trans. Energy Convers.* **2014**, *29*, 793–801. [[CrossRef](#)]
9. Strunz, K.; Abbasi, E.; Huu, D.N. DC Microgrid for Wind and Solar Power Integration. *IEEE J. Emerg. Sel. Top. Power Electron.* **2014**, *2*, 115–126. [[CrossRef](#)]
10. Mahmood, M.S.; Mahmood, S. Cost effective optimal solution for hybrid power system among diverse sources of renewable energy. In Proceedings of the TENCON 2017—2017 IEEE Region 10 Conference, Penang, Malaysia, 5–8 November 2017; pp. 1214–1215.
11. Pilz, M.; Al-Fagih, L. Recent Advances in Local Energy Trading in the Smart Grid Based on Game-Theoretic Approaches. *IEEE Trans. Smart Grid* **2019**, *10*, 1363–1371. [[CrossRef](#)]
12. Xu, X.; Yan, Z.; Shahidehpour, M.; Wang, H.; Chen, S. Power System Voltage Stability Evaluation Considering Renewable Energy with Correlated Variabilities. *IEEE Trans. Power Syst.* **2018**, *33*, 3236–3245. [[CrossRef](#)]
13. IEEE. 1668–2017—IEEE Recommended Practice for Voltage Sag and Short Interruption Ride-Through Testing for End-Use Electrical Equipment Rated Less than 1000 V; IEEE Std 1668–2017; Revision of IEEE Std 1668–2014; IEEE: Piscataway, NJ, USA, 2017.
14. Tu, C.; Guo, Q.; Jiang, F.; Chen, C.; Li, X.; Xiao, F.; Gao, J. Dynamic Voltage Restorer with an Improved Strategy to Voltage Sag Compensation and Energy Self-Recovery. *CPSS Trans. Power Electron. Appl.* **2019**, *4*, 219–229. [[CrossRef](#)]
15. Jiang, T.; Zhang, J.; Wu, X.; Sheng, K.; Wang, Y. A Bidirectional LLC Resonant Converter with Automatic Forward and Backward Mode Transition. *IEEE Trans. Power Electron.* **2015**, *30*, 757–770. [[CrossRef](#)]
16. Callegaro, L.; Ciobotaru, M.; Pagano, D.J.; Turano, E.; Fletcher, J.E. A simple smooth transition technique for the noninverting buck-boost converter. *IEEE Trans. Power Electron.* **2018**, *33*, 4906–4915. [[CrossRef](#)]
17. Tang, Y.; Chen, Y.; Madawala, U.K.; Thrimawithana, D.J.; Ma, H. A New Controller for Bidirectional Wireless Power Transfer Systems. *IEEE Trans. Power Electron.* **2018**, *33*, 9076–9087. [[CrossRef](#)]
18. Xu, J. PWM modulation and control strategy for LLC-DCX converter to achieve bidirectional power flow in facing with resonant parameters variation. *IEEE Access* **2019**, *7*, 54693–54704. [[CrossRef](#)]
19. Zhu, R.; Hoffmann, F.; Vázquez, N.; Wang, K.; Liserre, M. Asymmetrical bidirectional DC-DC converter with limited reverse power rating in smart transformer. *IEEE Trans. Power Electron.* **2020**, *35*, 6895–6905. [[CrossRef](#)]
20. Kwon, M.; Choi, S. Control Scheme for Autonomous and Smooth Mode Switching of Bidirectional DC–DC Converters in a DC Microgrid. *IEEE Trans. Power Electron.* **2018**, *33*, 7094–7104. [[CrossRef](#)]

21. Liserre, M.; Sauter, T.; Hung, J. Future energy systems: Integrating renewable energy sources into the smart power grid through industrial electronics. *IEEE Trans. Ind. Electron.* **2010**, *4*, 18–37. [[CrossRef](#)]
22. Huang, A.Q.; Crow, M.L.; Heydt, G.T.; Zheng, J.P.; Dale, S.J. The future renewable electric energy delivery and management system: The energy internet. *Proc. IEEE* **2011**, *99*, 133–148. [[CrossRef](#)]
23. Inoue, S.; Akagi, H. A bidirectional dc–dc converter for an energy storage system with galvanic isolation. *IEEE Trans. Power Electron.* **2007**, *22*, 2299–2306. [[CrossRef](#)]
24. Tan, N.M.L.; Abe, T.; Akagi, H. Design and performance of a bidirectional isolated dc–dc converter for a battery energy storage system. *IEEE Trans. Power Electron.* **2012**, *27*, 1237–1248. [[CrossRef](#)]
25. She, X.; Huang, A.Q.; Lukic, S.; Baran, M.E. On integration of solid state transformer with zonal dc microgrid. *IEEE Trans. Smart Grid* **2012**, *2*, 975–985. [[CrossRef](#)]
26. Babu, T.S.; Vasudevan, K.R.; Ramchandaramurthy, V.K.; Sani, S.B.; Chemud, S.; Lajim, R.M. A Comprehensive Review of Hybrid Energy Storage Systems: Converter Topologies, Control Strategies and Future Prospects. *IEEE Access* **2020**, *8*, 148702–148721. [[CrossRef](#)]
27. Cornea, O.; Andreescu, G.; Muntean, N.; Hulea, D. Bidirectional Power Flow Control in a DC Microgrid through a Switched-Capacitor Cell Hybrid DC–DC Converter. *IEEE Trans. Ind. Electron.* **2017**, *64*, 3012–3022. [[CrossRef](#)]
28. Ravi, D.; Reddy, B.M.; Letha, S.S.; Samuel, P. Bidirectional dc to dc Converters: An Overview of Various Topologies, Switching Schemes and Control Techniques. *Int. J. Eng. Technol.* **2018**, *7*, 360–365. [[CrossRef](#)]
29. Gorji, S.A.; Sahebi, H.G.; Ektesabi, M.; Rad, A.B. Topologies and Control Schemes of Bidirectional DC-DC Power Converters: An Overview. *IEEE Access* **2019**, *7*, 117997–118019. [[CrossRef](#)]
30. Swaminathan, N.; Cao, Y. An Overview of High-Conversion High-Voltage DC-DC Converters for Electrified Aviation Power Distribution System. *IEEE Trans. Transp. Electrif.* **2020**, *6*, 1740–1754. [[CrossRef](#)]
31. Xu, Q.; Vafamand, N.; Chen, L.; Dragičević, T.; Xie, L.; Blaabjerg, F. Review on Advanced Control Technologies for Bidirectional DC/DC Converters in DC Microgrids. *IEEE J. Emerg. Sel. Top. Power Electron.* **2021**, *9*, 1205–1221. [[CrossRef](#)]
32. Farhath, K.P.; Jayanand, B. Transformerless high step up dc-dc cascode converter with maximum power point tracking. In Proceedings of the 2015 International Conference on Power, Instrumentation, Control and Computing (PICC), Thrissur, India, 9–11 December 2015; pp. 1–6.
33. Liu, W.-S.; Chen, J.-F.; Liang, T.-J.; Lin, R.-L.; Liu, C.-H. Analysis, Design, and Control of Bidirectional Cascoded Configuration for a Fuel Cell Hybrid Power System. *IEEE Trans. Power Electron.* **2010**, *25*, 1565–1575.
34. Ho, C.N.; Chung, H.S.H.; Au, K.T.K. Design and implementation of a fast dynamic control scheme for capacitor supported dynamic voltage restorers. *IEEE Trans. Power Electron.* **2008**, *23*, 237–251. [[CrossRef](#)]
35. Thummala, P.; Maksimovic, D.; Zhang, Z.; Andersen, M.A.E. Digital Control of a High-Voltage (2.5 kV) Bidirectional DC-DC Flyback Converter for Driving a Capacitive Incremental Actuator. *IEEE Trans. Power Electron.* **2016**, *31*, 8500–8516. [[CrossRef](#)]
36. Chen, G.; Lee, Y.; Hui, S.; Xu, D.; Wang, Y. Actively Clamped Bidirectional Flyback Converter. *IEEE Trans. Ind. Electron.* **2000**, *47*, 770–779. [[CrossRef](#)]
37. Qian, T.; Song, W.; Lehman, B. Self-Driven Synchronous Rectification Scheme for Wide Range Application of DC/DC Converters with Symmetrically Driven Transformers. In Proceedings of the IEEE Power Electronics Specialists Conference, Jeju, Korea, 18–22 June 2006.
38. Ribeiro, E.; Cardoso, A.J.M.; Boccaletti, C. Fault Diagnosis in Non-isolated Bidirectional Half-bridge DC-DC Converters. In Proceedings of the IECON 2014—40th Annual Conference of the IEEE Industrial Electronics Society, Dallas, TX, USA, 29 October–1 November 2014; pp. 4458–4463.
39. Odo, P. A Comparative Study of Single-phase Non-isolated Bidirectional DC-DC Converters Suitability for Energy Storage Application in a dc Microgrid. In Proceedings of the 2020 IEEE 11th International Symposium on Power Electronics for Distributed Generation Systems (PEDG), Dubrovnik, Croatia, 28 September–1 October 2020; pp. 391–396.
40. Teng, J.; Chen, S.; Luan, S.; Xu, J. Bidirectional DC-DC Converter with a Wide-Range Voltage Conversion Ratio. In Proceedings of the 2019 IEEE 4th International Future Energy Electronics Conference (IFEEEC), Singapore, 25–28 November 2019; pp. 1–6.
41. Ahmad, A.; Beig, A.R.; Alsawalhi, J.; Jaafari, K.A. A Novel High Gain Bidirectional DC-DC Converter. In Proceedings of the 2020 IEEE Industry Applications Society Annual Meeting, Detroit, MI, USA, 10–16 October 2020; pp. 1–6.
42. Mukhtar, N.M.; Lu, D.D.C. A Bidirectional Flyback Converter with Cross-Coupled Non-Dissipative Snubber Circuits. In Proceedings of the IEEE International Telecommunications Energy Conference, Broadbeach, QLD, Australia, 22–26 October 2017.
43. Yang, L.; Liang, T. Analysis and Implementation of a Novel Bidirectional DC-DC Converter. *IEEE Trans. Ind. Electron.* **2012**, *59*, 422–434. [[CrossRef](#)]
44. Yamamoto, K.; Hiraki, E.; Tanaka, T.; Nakaoka, M.; Mishima, T. Bidirectional DC–DC Converter with Full-Bridge/Push-Pull Circuit for Automobile Electric Power Systems. In Proceedings of the 37th IEEE Power Electronics Specialists Conference, Jeju, Korea, 18–22 June 2006.
45. Chan, Y.P.; Loo, K.H.; Lai, Y.M. SVM-Plus-Phase-Shift Modulation Strategy for Single-Stage Immittance-Based Three-Phase AC-DC Bidirectional Converter. In Proceedings of the 19th European Conference on Power Electronics and Applications, Warsaw, Poland, 11–14 September 2017.
46. Lin, B.R.; Chen, J.J.; Hsieh, F.Y. Analysis and Implementation of a Bidirectional Converter with High Conversion Ratio. In Proceedings of the IEEE International Conference on Industrial Technology, Chengdu, China, 21–24 April 2008.

-
47. Elsayad, N.; Moradisizkoochi, H.; Mohammed, O.A. A new hybrid structure of a bidirectional DC-DC converter with high conversion ratios for electric vehicles. *IEEE Trans. Veh. Technol.* **2020**, *69*, 194–206. [[CrossRef](#)]
 48. Chen, B.Z.; Liao, H.; Chen, L.; Chen, J.F. Design and Implementation of the Bidirectional DC-DC Converter with Rapid Energy Conversion. *Energies* **2022**, *15*, 898. [[CrossRef](#)]